nature astronomy

Article

https://doi.org/10.1038/s41550-026-02857-y

The emerging timescale of young star clusters regulated by cluster stellar mass

Received: 31 October 2025

Accepted: 7 April 2026

Published online: 06 May 2026

Check for updates

Alex Pedrini[1] ✉, Angela Adamo[1] ✉, Daniela Calzetti[2,20], Arjan Bik[1,20], Thomas J. Haworth[3,20], Bruce G. Elmegreen[4,20], Mark R. Krumholz[5,20], Sean T. Linden[6,20], Benjamin Gregg[2,20], Helena Faustino Vieira[1,20], Varun Bajaj[7,20], Jenna E. Ryon[7,20], Ahmad A. Ali[8,20], Eric P. Andersson[9,20], Giacomo Bortolini[1,20], Michele Cignoni[10,11,12,20], Ana Duarte-Cabral[13,20], Kathryn Grasha[14,15,20], Natalia Lahén[16,17,20], Thomas S.-Y. Lai[18,20], Drew Lapeer[2,20], Matteo Messa[12,20], Göran Östlin[1,20], Elena Sabbi[19,20], Linda J. Smith[7,20] & Monica Tosi[12,20]

Quantifying the timescales of star cluster emergence from their natal clouds remains one of the main challenges in understanding the star formation process. These timescales are fundamental measurements of the star formation cycle within galaxies, yet are difficult to constrain due to the complex interplay between stellar feedback and star formation across multiple physical scales. Here we present Hubble Space Telescope and James Webb Space Telescope observations of thousands of young star clusters in four nearby galaxies (M51, M83, NGC 628 and NGC 4449). A substantial fraction of these clusters are still embedded within their natal gas and remain invisible at optical wavelengths. We constrain their emergence process by measuring the timescales required to disperse the surrounding material. We find a strong correlation between dispersal timescale and cluster stellar mass, with massive clusters emerging faster than their lower-mass counterparts. This is a critical constraint on star formation and stellar feedback simulations, which struggle to fully reproduce star clusters formation and emergence. Our results emphasize the central role of massive clusters in driving the escape of ionizing radiation into the galactic medium. Finally, they impose time limitations for planet formation in massive cluster environments where disks get exposed to ultraviolet irradiation and further gas infall is halted.

Star formation is generally understood to occur through the gravitational collapse of high-density regions in giant molecular clouds, leading to the formation of clustered stellar systems[1]. In star clusters and associations, massive stars ($M > 15$ masses of the Sun ($M_\odot$)) are responsible for the vast majority of energy and momentum released into the surrounding medium through a combination of processes, commonly referred to as stellar feedback, which leads to the destruction of their natal cloud (photoionization, stellar winds, radiation pressure and supernovae). Stellar feedback is thus one of the main processes believed to explain the observed inefficiency of star formation in galaxies, where only fractions of the available gas will ever form stars (for example, ref. 2). However, the timescale by which feedback drives cloud dispersal and its dependence on both star cluster properties and the surrounding environment remain poorly understood.

In recent years, numerical simulations have made substantial progress in incorporating the key physical processes necessary to study cluster formation and evolution (refs. 3–8, among many others). This has led to major advances in modelling observations of young star

A full list of affiliations appears at the end of the paper. ✉e-mail: alex.pedrini@astro.su.se; angela.adamo@astro.su.se

https://doi.org/10.1038/s41550-026-02857-y

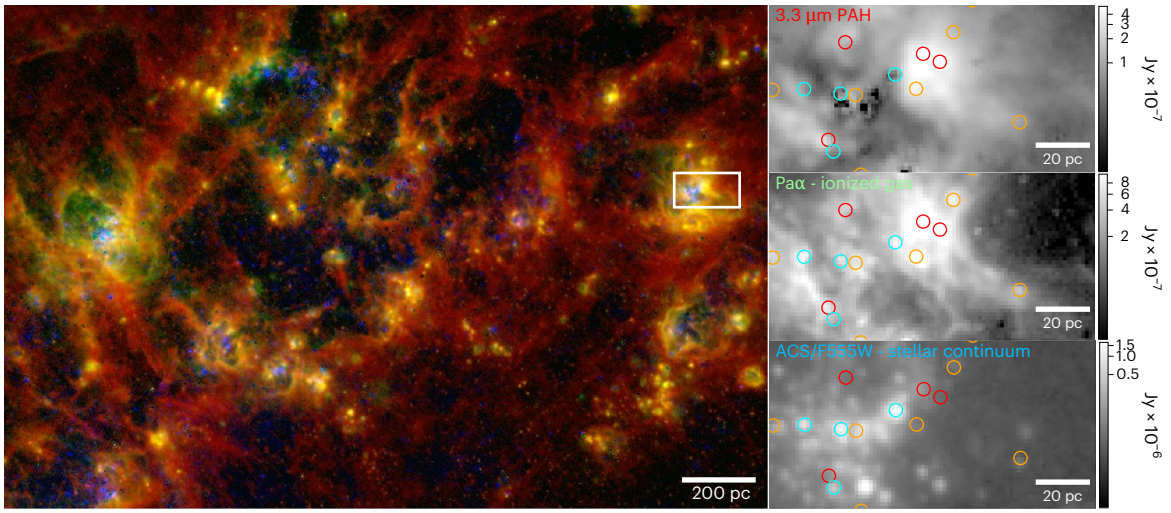

Fig. 1 | A kpc-scale star-forming complex in M51. Left: RGB composite image of the complex observed with HST and JWST. The blue channel traces stellar optical emission from the HST ACS/F555W filter, the green channel shows ionized emission from the Brα recombination line (JWST F405N, continuum-subtracted) and the red channel displays 3.3-μm PAH emission observed with JWST F335M (continuum-subtracted). The white box indicates the region shown in the right panels. Right: monochromatic maps of the zoomed-in region highlighted by the white box. From top to bottom: 3.3-μm PAH, Paα and ACS/F555W. Positions of eYSCs and optically detected YSCs are marked with red, orange and cyan circles for eYSCI, eYSCII and oYSCs, respectively. In M51, photometry of these clusters has been performed at a spatial scale of 5.8 pc. The eYSC and oYSC classification is described in the Results.

clusters (YSCs) and in understanding the detailed role of feedback in shaping their evolution and emergence. Nevertheless, many aspects of the star formation process across different physical scales remain uncertain, and even the most sophisticated galaxy simulations still struggle to fully reproduce the life cycle of star clusters.

From an observational perspective, estimating the emerging timescales of YSCs in both the Milky Way and the Local Volume (distance < 10 Mpc) has been challenging. In the Milky Way, line-of-sight confusion, obscuration and the intrinsic complexity of individual systems hinder a statistical and general interpretation. Until recently, extragalactic observations have only been able to resolve tracers of star formation and cold molecular gas (for example, Hα and CO emission) on the physical scales of star-forming complexes (~100 pc, refs. 9–12), but not down to the parsec scales necessary to detect single molecular clouds and star clusters.

The excellent sensitivity and resolution of the Hubble Space Telescope (HST) and the James Webb Space Telescope (JWST) enable us to map populations of YSCs in nearby galaxies and their associated star-forming regions, thus providing constraints on their emerging sequence. With the advent of JWST, several surveys have been characterizing populations of dusty emerging YSCs (eYSCs) in nearby galaxies[13–18]. These clusters show prominent ionized hydrogen and 3.3-μm polycyclic aromatic hydrocarbon (PAH) emission, which trace their evolutionary stages[16,17,19].

In Fig. 1, we show a representative example of complex star-forming regions in M51 observed with HST and JWST. The gas in the proximity of YSCs (~1–7 Myr old) where massive stars are located is ionized by very energetic photons ($E > 13.6$ eV) and emits in the Brα-4.05 μm recombination line (continuum-subtracted F405N filter; Fig. 1, green channel). After the ionization front, far-ultraviolet (UV) photons permeate the medium, dissociating molecular hydrogen and exciting PAH molecules[20,21], which dominate the mid-infrared spectra of photo-dissociation regions (PDRs). In particular, the 3.3-μm PAH emission (continuum-subtracted F335M filter; Fig. 1, red channel) traces PDRs at the same physical resolution as the hydrogen recombination lines.

In this work, we take advantage of extensive JWST and HST multi-wavelength campaigns to constraint the emerging timescales of star clusters from a deeply embedded phase to a optically exposed state at physical scales of 4–8 pc. We use the morphology of H II regions and PDRs surrounding eYSCs to establish an evolutionary sequence and constrain the relative ages of the different emergence stages as a function of the stellar masses of the clusters.

Table 1 | Number of eYSCI, eYSCII and oYSCs identified in four galaxies from the FEAST sample

	M51	M83	NGC 628	NGC 4449
eYSCI	1,589	1,001	636	211
eYSCII	768	429	512	229
oYSCs	664	1,201	1,495	162

We note that the number of eYSCs differs from that reported in ref. 23, due to the additional χ^2_{red} cut ($\chi^2_{red} < 50$) and correction for duplicates; systems that are identified both as eYSCs and oYSCs are removed from the eYSC classes and retained as oYSCs.

Results

We used JWST/NIRCam observations to identify eYSCs on 4–8-pc scales in four nearby galaxies from the Feedback in Emerging extrAgalactic Star clusTers (FEAST, principal investigator A.A., #1783) sample: M51, M83, NGC 628 (M74), NGC 4449. These galaxies have been selected to span various galactic environments and metallicities. Furthermore, we used archival HST imaging to identify optical YSCs (oYSCs) at the same spatial scale of the eYSCs. We then define three classes of YSCs based on the following identification criteria:

- eYSCI: eYSCs identified as compact and bright sources in the Paα/Brα emission lines and in the 3.3-μm PAH feature (Fig. 1, red circles). These objects still show compact H II regions and PDRs associated with the stellar component.
- eYSCII: in this case, we do not observe a compact 3.3-μm PAH feature, even if emission is observed. However, we still detect compact and bright Paα/Brα emission (Fig. 1, orange circles).
- oYSC: optically selected star clusters (bright sources in V band, ACS/F555W) younger than 10 Myr (Fig. 1, blue circles) based on spectral energy distribution (SED) fitting outputs, introduced below.

We refer to the Methods for a complete description of all the analysis steps leading to the creation of final catalogues. In general, source

https://doi.org/10.1038/s41550-026-02857-y

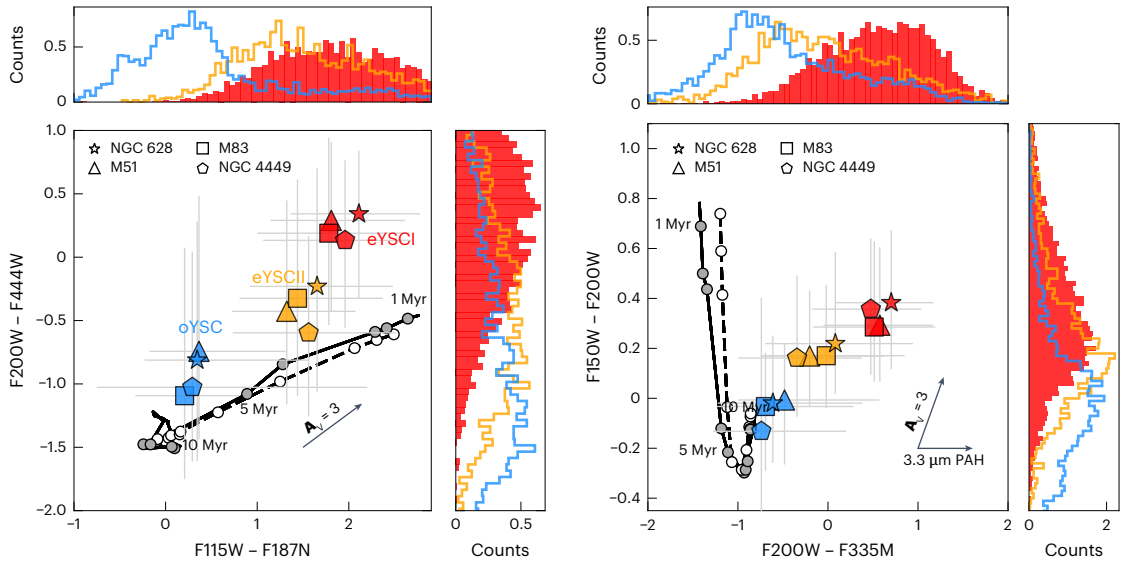

Fig. 2 | The NIR colours of eYSCs and oYSCs. Left: NIR colour–colour diagram of the eYSC and oYSC populations in the four FEAST galaxies. Units are AB mag. Redder colours along the *y* axis trace hot dust emission through the F444W filter, while along the *x* axis the F187N filter shifts younger objects to redder colours owing to bright Paα emission. Symbols show the median values for the four galaxies, colour-coded by cluster class: red, orange, and blue for eYSCI, eYSCII, and oYSCs, respectively. Error bars represent the 16th–84th percentiles of each distribution. Histograms display the combined distributions (normalized counts), also colour-coded by cluster class. The evolutionary tracks are taken from the `yggdrasil` single stellar population synthesis code (solid) and `CIGALE` (dashed), with nebular emission and no dust absorption or emission, as described in the text. The extinction vector is from ref. 78. Right: the same as the left panel, but with a different colour combination. Here, the *y* axis (F150W-F200W) serves as a proxy for YSC age, as indicated by the evolutionary track. The *x* axis traces bright emission from the 3.3-μm PAH feature, displayed as an excess in the F335M filter.

extraction and identification was followed by multiband photometry across all available HST and JWST bands. SED fitting was then performed on the selected clusters using `CIGALE` (Code Investigating GALaxy Emission)[22], yielding physical parameters for the entire population of eYSCs and oYSCs, including age, stellar mass and extinction. Both the photometric measurements and the SED fitting procedure are described in details in ref. 23 and are summarized in the Methods. For each class and galaxy, we report the total number of selected cluster candidates in each category in Table 1.

In Fig. 2, we present the near-infrared (NIR) colours for eYSCs and oYSCs. For each galaxy and emergence class, we show the median colour values (symbols, eYSCI in red, eYSCII in orange and oYSCs in blue) and the 16th–84th percentile ranges of each sample distribution (bars). We also display histograms of the combined distributions for the four galaxies at the top and right side of each plot. In both panels, the median points and the histograms reveal three distinct populations corresponding to the three classes. The solid and dashed evolutionary tracks are extracted from `yggdrasil`[24] and `CIGALE`, respectively, and represent single stellar populations based on Starburst99/Padova-AGB[25] models versus BC03[26] stellar tracks, respectively. Both models include nebular emission treatment[27] assuming a covering fraction of 0.5, solar metallicity, no extinction and no dust emission. Although `CIGALE` includes dust and PAH emission in our standard set-up (Methods), these components were intentionally switched off for this figure to produce dust-free reference tracks, consistent with the assumptions adopted for the `yggdrasil` models.

In all galaxies investigated in this work, the median colours of the three classes show the same trend in both panels. The youngest class (eYSCI, red symbols) shows the largest excess in Paα and in the redder F444W filter, which trace both ionized gas and emission from hot dust (Fig. 2, top), as well as in 3.3-μm emission and dust extinction (Fig. 2, bottom). The eYSCII (orange symbols) are an intermediate stage of emergence. They still present notable excess emission from hot dust and PAHs, causing their colours to deviate from the dust-free model tracks, even when accounting for dust extinction ($\mathbf{A}_V$ vector). By contrast, oYSCs populate regions of the NIR diagrams consistent with older ages (7–10 Myr), moderate dust extinction, and no or minimal dust emission. The NIR colours of these three different classes of star clusters therefore reveal an evolutionary sequence observed in all the studied galaxies: eYSCI → eYSCII → oYSCs, which we later use to quantify the timescales of cluster emergence.

In general, the `CIGALE` results reinforce the observed evolutionary sequence of Fig. 2, with star clusters becoming older and less reddened when moving from eYSCI to oYSCs[16]. However, as shown in a recent study[23], systematic uncertainties in the absolute ages recovered from SED fitting affect the timescale analysis. We therefore use relative numbers of clusters in the different emergence stages to derive the emerging timescales. We define the emerging timescale $\tau_{\rm TOT}$ as the period required for clusters with associated H II regions (eYSCI and eYSCII) to evolve into exposed oYSCs, such as total gas removal. This timescale is given by the following:

$$\tau_{\rm TOT} = \frac{\#\text{eYSCI} + \#\text{eYSCII}}{\#\text{eYSCI} + \#\text{eYSCII} + \#\text{oYSC}} \times 10\,\text{Myr}, \qquad (1)$$

where the number sign defines the number of clusters in each class. We note that eYSCs overlapping in position with optically identified sources are counted only as oYSCs (Methods). We also define the PDR timescale $\tau_{\rm PDR}$ as the period over which eYSCI lose their compact PDRs, traced by the 3.3-μm PAH emission. This would correspond to the most embedded phase and is estimated as

$$\tau_{\rm PDR} = \frac{\#\text{eYSCI}}{\#\text{eYSCI} + \#\text{eYSCII} + \#\text{oYSC}} \times 10\,\text{Myr}. \qquad (2)$$

Details of this method and the derivation of these timescales are presented in the Methods. In defining these timescales, our starting point is the onset of photoionization by massive stars of the surrounding neutral hydrogen, traced by Paα emission. The earlier, deeply embedded phase, during which clusters remain obscured and the ionizing flux is not yet detectable, cannot be probed with our data and is expected to be very short ($\lesssim$1–2 Myr)[16,28,29].

Figure 3 shows the median of $\tau_{\rm TOT}$ (filled circles) and $\tau_{\rm PDR}$ (unfilled squares) timescales, as a function of the logarithm of stellar mass for the

https://doi.org/10.1038/s41550-026-02857-y

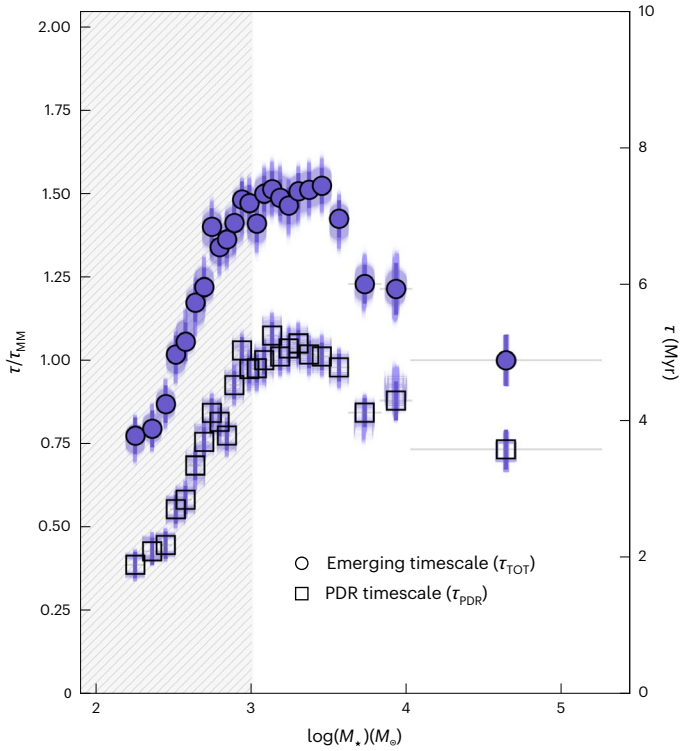

Fig. 3 | Emerging timescales as a function of stellar mass in log scale for the combined population of YSCs in the four FEAST galaxies. Filled circles and open squares indicate the τ_{TOT} and τ_{PDR} timescales, respectively. Each bin contains the same number of objects, except for the largest two mass bins, which are split into two additional bins as described in the text; mass binning is further detailed in the Methods. On the *y* axis, τ/τ_{MM} shows timescales normalized to the τ_{TOT} of the highest mass bin (τ_{MM} = 4.9 Myr), while the secondary *y* axis gives absolute values. Shadowed areas beneath the measurements show the timescales re-estimated by randomly sampling the ages of the oYSCs (Methods), confirming the observed trends. The *y* error bars show Poisson uncertainties (set by the number of sources in each bin), and the *x* error bars indicate the bin widths. Below $10^3\,M_\odot$, results are affected by completeness limits; this region is shaded in grey.

combined populations of YSCs (~8,900 clusters) in the four observed galaxies. Each mass bin contains the same number of objects (356). Because the number of clusters with masses above ~$10^4\,M_\odot$ is small, the highest mass bin spans most of the upper end of the distribution. To avoid having one excessively wide bin, we subdivided it into two additional bins of 188 clusters. This improves the temporal sampling while still ensuring a statistically significant number of clusters in each phase. We further assessed the impact of uncertainties in the physical properties (from the CIGALE fits) on the recovered trend by propagating errors through Monte Carlo sampling, shown as shaded areas underlying the measurements. The cluster sample is complete above $10^3\,M_\odot$ (ref. 23). The grey-shaded region indicates lower masses where incompleteness affects the sample.

On the right *y* axes, we plot absolute timescales from equations (1) and (2), and on the left *y* axes the normalized timescales to the value recovered for the τ_{TOT} in the highest mass bin (blue circle corresponding to τ_{MM} = 4.9 Myr and τ/τ_{MM} = 1). While the absolute timescale will somewhat depend on the maximum age assumed to select YSCs and fit eYSCs (10 Myr), the relative timescale enhances the differences as a function of cluster stellar mass.

Above $10^3\,M_\odot$ (where detection is complete at all emergence stages), we find a strong trend with stellar mass, where massive clusters τ_{TOT} (filled circle) emerge faster (~5 Myr) than less massive τ_{TOT} (~7–8 Myr). Clusters in the low-mass bins are about 1.5 times slower than the most massive clusters to complete the emerging sequence. Moreover, high-mass clusters spend most of their emerging phase (~75% of the time, ~4 Myr, open squares) associated to a compact PDR traced by 3.3-μm emission, whereas low-mass clusters stay associated with a compact PDR for ~65% (~5 Myr) of their total emerging timescale (7–8 Myr). This implies that, after losing their PDR, low-mass clusters require a relatively longer time to complete their emergence than their massive counterparts (difference between circles and squares at each mass bin).

Figure 4 presents the timescale analysis for each galaxy, confirming the general trends observed in Fig. 3. However, it also reveals differences among galaxies. M51 shows the longest timescales, with emerging timescales peaking at ~9 Myr for clusters in the low-mass bin, possibly affected by complex galactic dynamics due to ongoing tidal interactions with a satellite galaxy[30]. M83 and NGC 628 follow more closely the overall population trend, although in NGC 628 the contrast between low- and high-mass bins is less pronounced, with comparable timescales across bins. Differences in the recovered emerging timescales among the three spirals might arise from variations in their cluster birth environments, gas surface densities, cloud mass spectra and dynamical conditions (for example, shear, bars and shocks). Interestingly, NGC 4449, the low-metallicity target (1/3 solar metallicity, $Z_\odot$)[31]), exhibits much shorter τ_{PDR} than the other three spirals. Ref. 32 reports a deficit of PAHs in this galaxy, possibly due to the limited formation of these molecules in such environments and/or their destruction, as also confirmed by recent analyses of other low-metallicity targets (for example, ref. 33). Similarly, ref. 34, using HST/far-UV observations of NGC 4449, found that stars and clusters do not exhibit a UV bump at 217.5 nm in regions with intense UV radiation, suggesting rapid disruption.

The results presented in this work rely on the assumption that the derived stellar mass does not increase significantly during the emergence process, because we select star clusters already associated with compact H II regions. This assumption is reinforced by observations of YSCs in the Milky Way at similar physical scales as in this study, where their member stars present an age spread of less than 1 Myr, suggesting that cluster assembly occurs on short timescales[35,36].

However, simulations that account for stellar dynamics in emerging star clusters suggest that between 5% and 20% of the stellar mass may be lost during these initial stages (for example, refs. 37,38). In the Methods, we present tests investigating the impact of stellar mass loss by considering two extreme scenarios in which eYSCs lose 20% and 50% of their total stellar mass before they become YSCs (Extended Data Fig. 1). Even under these extreme assumptions, our findings show that the mass trend is preserved.

We additionally tested the robustness of the mass–emergence timescale relation by removing each galaxy in turn, and the trend persisted. Finally, to avoid potential biases from SED fitting, we analysed the emerging timescales as a function of cluster luminosity in broad band NIR filters. The general trends remain unchanged when timescales are plotted against stellar continuum luminosity (Extended Data Fig. 2).

Discussion

In recent years, several studies have investigated the emergence of star formation at larger physical scales (~25–150 pc) by analysing the spatial decorrelation of tracers of different interstellar medium (ISM) phases[10–12,29,39,40]. Ref. 11 reported timescales for 17 galaxies of the overlapping phase between Hα and PAH tracers (for example, 7.7 μm), which can be thought of as a proxy for our τ_{PDR}. The authors found a median value of 6 ± 1 Myr, slightly higher than our results for this timescale (4–5 Myr depending on the specific mass bin; Fig. 3), although still within the uncertainties. At star cluster scales, other JWST studies have reported timescales equal or shorter than 5 Myr for their PDR-dominated phase[13–15,17], consistent with the average values found in this work. However, none of these studies explored the dependence of the emerging timescales as a function of cluster stellar mass. In our

https://doi.org/10.1038/s41550-026-02857-y

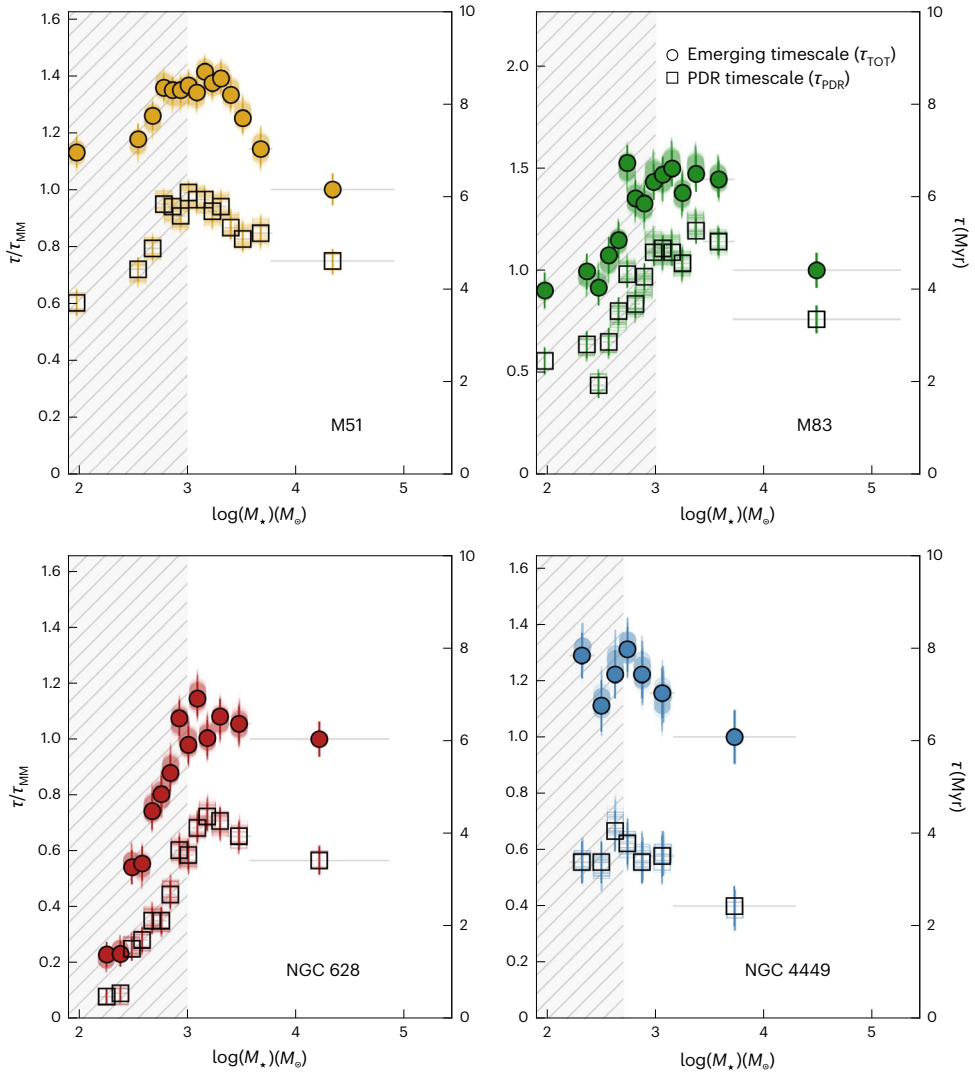

Fig. 4 | Emerging timescale as a function of stellar mass in log scale for YSCs in the four FEAST galaxies individually. M51 (top left), M83 (top right), NGC 628 (bottom left) and NGC 4449 (bottom right). For each galaxy, filled circles and open squares indicate the τ_{TOT} and τ_{PDR} timescales, respectively. Each bin contains the same number of objects. On the *y* axis, τ/τ_{MM} shows timescales normalized to the τ_{TOT} of the highest mass bin of each galaxy, while the secondary *y* axis gives absolute values. Shadowed areas beneath the measurements show the timescales re-estimated by randomly sampling the ages of the oYSCs (Methods), confirming the observed trends. The *y* error bars show Poisson uncertainties (set by the number of sources in each bin), and the *x* error bars indicate the bin widths. Below $10^3\,M_\odot$, results are affected by completeness limits; this region is shaded in grey. In NGC 4449, masses are affected by completeness limits below $10^{2.75}\,M_\odot$ (ref. 23).

study, we provide a unique galaxy-wide, cluster-scale census of embedded to exposed phases linking emergence timescales to mass across star-forming galaxies representative of the range observed in the Local Volume. Massive clusters clear faster, implying earlier UV leakage and reduced gas replenishment time at precisely the sites that dominate a galaxy's ionizing budget. The timescales recovered in this study confirm that pre-supernova feedback plays a pivotal role in pre-processing the gas, before the explosion of the first supernovae[41]. During τ_{PDR}, radiation pressure drives the expansion of H II regions[42–44], which in turn disperse the surrounding PDRs. Our recovered total timescales, τ_{TOT}, are consistent with the expected timing of supernovae, with the observed decreasing trend with mass supporting a scenario in which the supernova delay time is longer for lower-mass YSCs[10].

The cluster masses analysed in this work rely on SED fitting estimates from CIGALE, which adopts a deterministic approach. However, stochastic initial mass function sampling effects become increasingly important at lower cluster masses[45]. We verified this explicitly by replacing the inferred mass with integrated NIR luminosity and found that the same trends persist (Extended Data Fig. 2), thus confirming that the recovered timescale dependence on cluster mass is reliable. The flattening and scatter of τ/τ_{MM} below ~$10^{3.5}\,M_\odot$ is driven by variable number of massive stars that start to affect the total cluster luminosity and the inferred stellar mass.

State-of-the-art numerical simulations of isolated clouds reach broad conclusions on the dependence of emerging timescales on star cluster mass. Initial conditions of the molecular gas clouds and implemented recipes for formation of stars and feedback treatment produce different outcomes[46]. Analyses of STARFORGE simulations[47,48] report longer emergence timescales for more massive clusters when they form in more massive but less dense molecular clouds. Other studies show that massive clusters achieve higher integrated star formation efficiency and emerge faster (dissolve their natal cloud more rapidly) if they form in increasingly denser clouds[5,7,49]. At high gas densities, radiation pressure on dust and gas becomes the main feedback mechanism responsible for emerging, allowing the expansion and then the dissolution of H II regions[7]. Although the starting points of simulations and our analysis differ (our detection is dictated by the presence of ionized hydrogen and PAH emission), our results might guide simulations towards assumptions that yield more realistic outputs and calibrate star cluster feedback for subresolution feedback models. Extragalactic

observations generally suggest an almost-flat trend between cluster size and mass[2]. Hence, by assuming that clusters in our analysis have similar sizes (in local galaxies, cluster sizes show log-normal distributions around 2–3 pc)[2], more massive star clusters are, on average, denser. If the higher stellar density reflects the initial density of the gas clumps from which the clusters formed, the trends we observe support a scenario in which massive star clusters do not simply form in more massive clouds, but in denser gas clumps, resulting in higher integrated star-formation efficiency and faster cloud-clearing timescales.

Because the number of massive stars and the mass of the most massive star scale with cluster mass (for example, ref. 50), it is expected that massive clusters dominate the production of ionizing photons in galaxies[51]. The key question we address here is how long it takes for clusters to emerge from their birth clouds. Until now, it has been unclear whether low- or high-mass clusters emerge faster, and how this affects ionizing photon production and escape. Our findings show that massive clusters clear their natal molecular clouds more rapidly, confirming them as the dominant accessible sources of ionizing photons in galaxies.

Furthermore, our results have important implications for the theory of planet formation. Planet-forming disks around stars are influenced by their immediate environment (for example, refs. 52,53). Noticeable differences are found in disk fractions near massive and dense star clusters, where UV photoevaporation and stellar encounters become dominant[54,55], with the most massive clusters ($M > 10^4\,M_\odot$) showing significantly lower disk fractions compared with lower-mass clusters of the same age. Recent observations and simulations (for example, refs. 56–60) have reported prolonged accretion from surrounding dense gas into disks. The shorter emergence timescales of massive clusters have the dual effect of exposing a larger fraction of disks to external photoevaporation and removing the mass reservoir for infall more rapidly. Achieving such an interpretation on a cluster-by-cluster basis in the Milky Way is challenging given the specifics and complexities of each system. However, our statistical sample of extragalactic clusters provides a more general and statistically robust framework. Our finding that massive clusters experience earlier decoupling between stars and gas is consistent with the observed lower disk fractions in massive clusters in the Milky Way, which would imply shorter timescales available for planet formation[61].

Methods

Observations and data reduction

In this work, we used publicly available HST UV-optical observations of M51, M83, NGC 628 and NGC 4449, as well as newly collected NIR observations with JWST. The properties of these galaxies are described in ref. 23. Moreover, an overview of the observed HST filters and the corresponding observing programmes can be found in table 2 of ref. 23. JWST NIRCam observations were obtained from the the Mikulski Archive for Space Telescopes (MAST) as part of the FEAST programme. These galaxies have been selected to span a range of distances between 4 Mpc and 10 Mpc, ensuring resolutions of a few parsec in the NIR emission coming from H II regions and PAHs in PDRs, as well as access to large field of views covering most of the galactic disks. They also encompass a broad range of galactic environments, including nuclear starbursts and molecular rings, as well as an interacting system, a low-pressure dwarf system and spiral galaxies with diverse arm morphologies. Our targets have been observed in the following filters: F115W, F150W, F187N, F200W, F300M (F277W in the case of NGC 628), F335M, F405N and F444W. The data have been reduced with the public pipeline (version 1.12.5 and calibration number 1169). Both HST and JWST images have been drizzled to a common scale of 0.04″ per pixel and aligned to the same reference system with GAIA[62]. To obtain emission maps of the Paα-1.87 μm hydrogen recombination line from the F187N filter, we subtracted the stellar continuum using the two adjacent filters F150W and F200W. The F200W also contains emission from the Paα line, and therefore we developed an iterative procedure to remove this additional component. Similarly, we used the F300M (or F277W in NGC 628) and the F444W to subtract stellar and dust continuum from the F335M and the F405N filters to obtain maps of the 3.3-μm PAH emission and the Brα recombination line. These procedures are fully described in refs. 63,64. Final science-ready mosaics and continuum-subtracted maps for the FEAST galaxies will be available at https://feast-survey.github.io.

Identification of eYSCs and oYSCs. We identified eYSC by the presence of compact and peaked emission in the Paα/Brα emission lines and in the 3.3-μm PAH maps. To do this, we performed aperture photometry from the visually selected clusters in all the available HST and JWST filters. The adopted method for the multiband photometry is fully described in ref. 16. We used radii of 5 pixels for the closer galaxies M83 and NGC 4449, corresponding to a physical radius of about 4.55 and 3.88 pc, respectively. For M51 and NGC 628, we used radii of 4 pixels, which corresponds to 5.8 and 7.8 pc, respectively. Clusters with a clear and compact detection in Paα and a compact 3.3-μm PAH counterpart are classified as eYSCI. Meanwhile, eYSCII do not show peaked emission in the 3.3-μm PAH. We adopted a 4-pixel matching criterion between the centres of the Paα and 3.3-μm PAH peaks for a source to be classified as an eYSCI. As described in ref. 16, a larger (5-pixel) matching criterion has been tested to verify the effect of this assumption in the distinction of eYSCI versus eYSCII. The changes across classes were negligible (a few per cent), and did not significantly affect the recovered timescales. oYSCs are selected in the HST/F555W filter and to be younger than 10 Myr, where cluster age is estimated from `CIGALE` (see the next section). The reader may find an in-depth summary of the selection process in refs. 16,19,23,63. After photometry, we applied a signal to noise (S/N) > 3 cut to eYSCI and eYSCII in all the NIRCam bands, to ensure good detection of these objects. Meanwhile, oYSCs are required to be well detected in at least four HST bands. In addition, a few per cent of the eYSCs were found to have a positional match with oYSCs. We removed these objects from the eYSC catalogues and retained them only in the YSC class.

Derivation of physical properties and emerging timescales

We derived physical properties of eYSC and oYSCs using the SED fitting code `CIGALE`. In short, for each star cluster, `CIGALE` uses a deterministic approach to find the set of physical models (stellar, nebular and dust) that best fits the observations. The goodness of the fitting process is measured by the reduced chi-square ($\chi^2_{\rm red}$). The entire fitting procedure, as well as the resulting distribution of the ages and masses of eYSC, is presented in ref. 23. After visual inspection of the SEDs, we applied a $\chi^2_{\rm red} < 50$ selection for all the fitted clusters to rule out the presence of large fit failures in the sample. The identification criteria for eYSC detection imply that these clusters are young, with ages below 10 Myr. Their mass ranges between $10^2\,M_\odot$ and $10^4\,M_\odot$, with a peak around $10^3\,M_\odot$, and the median attenuation values $E(B-V)$ vary from 0.6 mag in NGC 4449 and NGC 628 to 0.8 mag in M51 and M83. The authors of this paper recommend caution in relying on absolute age values due to the lack of available models that account for all the components necessary to fit YSCs in the NIR, such as stochastic sampling of the initial mass function, pre-main-sequence stars and hot dust. For this reason, in this Article, we estimated emerging timescales by leveraging a statistical approach that has been previously explored in the literature and does not involve single cluster age estimations[16,65]. We can count the fraction of clusters in the identified evolutionary phases (Fig. 2) and define the emerging timescale $\tau_{\rm TOT}$ introduced in equation (1). We adopted 10 Myr as a star-formation timescale, because the eYSC are fitted up to 10 Myr, due to the presence of ionized gas emission, and the oYSCs are selected to be younger than 10 Myr. We notice that our trends do not change if we use a different limit for the oYSCs ages (for example, 7 Myr or 15 Myr). Below ~$10^3\,M_\odot$ (shaded area), our results are sensitive to completeness limits and the positive trends for the emerging timescales might be due to more severe incompleteness in

individual cluster catalogues. Analogously, we can define a timescale necessary for eYSCI to become eYSCII, that is, the timescale for cluster to lose their compact PDR traced by 3.3-µm PAH emission. This is the τ_{PDR}, as defined in equation (2). With these definitions, we note that uncertainties on the recovered ages with CIGALE may lead to an incorrect estimation of the number of oYSCs younger than 10 Myr, which in turn affects the recovered timescales. To assess this effect, we re-estimated the emerging timescales with a Monte Carlo sampling, drawing ages of oYSCs from normal distributions centred on the original values with widths set by their age uncertainties. We repeated this procedure 1,000 times, and the resulting spread is shown as the shaded region underlying the measurements in Figs. 3 and 4.

The recovered emerging timescales are then illustrated as a function of stellar mass bins, which were chosen such that each bin contains the same number of clusters. For the combined dataset (Fig. 3), each bin contains 356 star clusters. Because only about 3% of the clusters have masses higher than $10^4\,M_\odot$, we further divided the most massive bin into two sub-bins of 188 sources each, as described in the Results. For the analysis of individual galaxies, each bin contains 199, 171, 165 and 74 clusters for M51, M83, NGC 628 and NGC 4449, respectively. For the single-galaxy cases, we did not apply any splitting to the high-mass bins.

Impact of stellar mass loss during the emerging process. In this analysis, by comparing the counts of eYSCs and oYSCs within the same mass bins to derive emerging timescales, we implicitly assume that the stellar mass remains constant during the emergence to the optical phase. This assumption warrants further investigation. Mass losses due to stellar evolution and ejection of stars due to strong dynamical interactions (for example, refs. 38,66–69) may be able to reduce the final mass of oYSCs by a non-negligible amount.

We test extreme scenarios in which mass is removed instantaneously, and eYSCs lose between 20% and 50% of their total stellar mass during their emergence into oYSCs. To perform this test, we repeated the analysis shown in Fig. 3 after multiplying eYSC stellar masses by factors of 4/5 (20% mass loss) and 1/2 (50% mass loss). With this approach, eYSC with stellar mass m_* are assigned to the same mass bins as oYSCs with masses 4/5 m_* and 1/2 m_*, respectively, thereby mimicking the effect of mass loss. We present the results of this analysis for the combined population of YSCs in Extended Data Fig. 1, where the left and right panels correspond to mass losses of 4/5 and 1/2, respectively. Under these assumptions, more massive clusters move faster towards short emerging timescales; however, the overall trend with cluster stellar mass is preserved.

Data availability

The data were obtained from the MAST at the Space Telescope Science Institute. The specific observations analysed are available at https://doi.org/10.17909/f4vm-c771 (ref. 70). All our data products are available via MAST as a High Level Science Product at https://doi.org/10.17909/6dc1-9h53 (ref. 71) and on the FEAST webpage (https://feast-survey.github.io/).

Code availability

This work made use of Astropy, a community-developed core Python package and an ecosystem of tools and resources for astronomy[72], NumPy[73], SciPy[74], Matplotlib[75], Pandas[76] and SAOImageDS9 (developed by the Smithsonian Astrophysical Observatory 2000)[77]. SED fits of star clusters were performed with the publicly available code CIGALE[22].

References

1. Lada, C. J. & Lada, E. A. Embedded clusters in molecular clouds. *Annu. Rev. Astron. Astrophys.* **41**, 57–115 (2003).
2. Krumholz, M. R., McKee, C. F. & Bland-Hawthorn, J. Star clusters across cosmic time. *Annu. Rev. Astron. Astrophys.* **57**, 227–303 (2019).
3. Grudić, M. Y. et al. The dynamics and outcome of star formation with jets, radiation, winds, and supernovae in concert. *Mon. Not. R. Astron. Soc.* **512**, 216–232 (2022).
4. Ali, A. A., Dobbs, C. L., Bending, T. J. R., Buckner, A. S. M. & Pettitt, A. R. Star cluster formation and feedback in different environments of a Milky Way-like galaxy. *Mon. Not. R. Astron. Soc.* **524**, 555–568 (2023).
5. Polak, B. et al. Massive star cluster formation: I. High star formation efficiency while resolving feedback of individual stars. *Astron. Astrophys.* **690**, A94 (2024).
6. Andersson, E. P., Mac Low, M.-M., Agertz, O., Renaud, F. & Li, H. Pre-supernova feedback sets the star cluster mass function to a power law and reduces the cluster formation efficiency. *Astron. Astrophys.* **681**, A28 (2024).
7. Menon, S. H., Burkhart, B., Somerville, R. S., Thompson, T. A. & Sternberg, A. Bursts of star formation and radiation-driven outflows produce efficient LyC leakage from dense compact star clusters. *Astrophys. J.* **987**, 12 (2025).
8. Lahén, N. et al. The formation, evolution, and disruption of star clusters with improved gravitational dynamics in simulated dwarf galaxies. *Mon. Not. R. Astron. Soc.* **538**, 2129–2148 (2025).
9. Grasha, K. et al. Connecting young star clusters to CO molecular gas in NGC 7793 with ALMA-LEGUS. *Mon. Not. R. Astron. Soc.* **481**, 1016–1027 (2018).
10. Chevance, M. et al. Pre-supernova feedback mechanisms drive the destruction of molecular clouds in nearby star-forming disc galaxies. *Mon. Not. R. Astron. Soc.* **509**, 272–288 (2022).
11. Kim, J. et al. Timescales of polycyclic aromatic hydrocarbon and dust continuum emission from gas clouds compared to molecular gas cloud lifetimes in PHANGS-JWST galaxies. *Astrophys. J.* **988**, 215 (2025).
12. Ramambason, L. et al. Duration and properties of the embedded phase of star formation in 37 nearby galaxies from PHANGS-JWST. *Astron. Astrophys.* **706**, A186 (2026).
13. Sun, J. et al. Hidden gems on a ring: infant massive clusters and their formation timeline unveiled by ALMA, HST, and JWST in NGC 3351. *Astrophys. J.* **967**, 133 (2024).
14. Linden, S. T. et al. GOALS-JWST: constraining the emergence timescale for massive star clusters in NGC 3256. *Astrophys. J. Lett.* **974**, L27 (2024).
15. Rodríguez, M. J. et al. Tracing the earliest stages of star and cluster formation in 19 nearby galaxies with PHANGS-JWST and HST: compact 3.3 µm polycyclic aromatic hydrocarbon emitters and their relation to the optical census of star clusters. *Astrophys. J.* **983**, 137 (2025).
16. Knutas, A. et al. FEAST: JWST uncovers the emerging timescales of young star clusters in M83. *Astrophys. J.* **993**, 13 (2025).
17. Whitmore, B. C. et al. Empirical SED templates for star clusters observed with HST and JWST: no strong PAH or IR dust emission after 5 Myr. *Astrophys. J.* **982**, 50 (2025).
18. Henny, K. F. et al. Star clusters in the near-ultraviolet-optical-near-infrared: spectral energy distribution modeling with direct markers of gas and dust emission. *Astrophys. J.* **991**, 76 (2025).
19. Pedrini, A. et al. FEAST: Feedback in Emerging extragAlactic Star ClusTers: JWST spots polycyclic aromatic hydrocarbon destruction in NGC 628 during the emerging phase of star formation. *Astrophys. J.* **971**, 32 (2024).
20. Allamandola, L. J., Tielens, A. G. G. M. & Barker, J. R. Interstellar polycyclic aromatic hydrocarbons: the infrared emission bands, the excitation/emission mechanism, and the astrophysical implications. *Astrophys. J. Suppl. Ser.* **71**, 733 (1989).
21. Tielens, A. G. G. M. Interstellar polycyclic aromatic hydrocarbon molecules. *Annu. Rev. Astron. Astrophys.* **46**, 289–337 (2008).

22. Boquien, M. et al. CIGALE: a python Code Investigating GALaxy Emission. *Astron. Astrophys.* **622**, A103 (2019).
23. Pedrini, A. et al. The near infrared spectral energy distribution of young star clusters in the FEAST galaxies: missing ingredients at 1–5 μm. *Astrophys. J.* **992**, 96 (2025).
24. Zackrisson, E., Rydberg, C.-E., Schaerer, D., Östlin, G. & Tuli, M. The spectral evolution of the first galaxies. I. James Webb Space Telescope detection limits and color criteria for population III galaxies. *Astrophys. J.* **740**, 13 (2011).
25. Vázquez, G. A. & Leitherer, C. Optimization of Starburst99 for intermediate-age and old stellar populations. *Astrophys. J.* **621**, 695–717 (2005).
26. Bruzual, G. & Charlot, S. Stellar population synthesis at the resolution of 2003. *Mon. Not. R. Astron. Soc.* **344**, 1000–1028 (2003).
27. Ferland, G. J. et al. The 2013 release of Cloudy. *Rev. Mexicana Astron. Astrofis.* **49**, 137–163 (2013).
28. Johnson, K. E., Indebetouw, R. & Pisano, D. J. Searching for embedded super-star clusters in IC 4662, NGC 1705, and NGC 5398. *Astron. J.* **126**, 101–112 (2003).
29. Corbelli, E. et al. From molecules to young stellar clusters: the star formation cycle across the disk of M 33. *Astron. Astrophys.* **601**, A146 (2017).
30. Dobbs, C. L., Theis, C., Pringle, J. E. & Bate, M. R. Simulations of the grand design galaxy M51: a case study for analysing tidally induced spiral structure. *Mon. Not. R. Astron. Soc.* **403**, 625–645 (2010).
31. Pilyugin, L. S., Grebel, E. K. & Zinchenko, I. A. On the radial abundance gradients in discs of irregular galaxies. *Mon. Not. R. Astron. Soc.* **450**, 3254–3263 (2015).
32. Gregg, B. et al. The calibration of short-wavelength polycyclic aromatic hydrocarbon emission as star formation rate indicators with JWST. *Astrophys. J.* **997**, 20 (2026).
33. Lai, T. S.-Y. et al. Resolving emission from small dust grains in the Blue Compact Dwarf II Zw 40 with JWST. *Astrophys. J. Lett.* **991**, L56 (2025).
34. Sabbi, E. et al. Galaxy UV Legacy Project: survey description and first insights Into NGC 4449 recent history of star formation. *Astrophys. J.* **1000**, 241 (2026).
35. Kudryavtseva, N. et al. Instantaneous starburst of the massive clusters Westerlund 1 and NGC 3603 YC. *Astrophys. J. Lett.* **750**, L44 (2012).
36. Da Rio, N. et al. A multi-color optical survey of the Orion Nebula Cluster. II. The H-R Diagram. *Astrophys. J.* **722**, 1092–1114 (2010).
37. Pfalzner, S. & Kaczmarek, T. Reaction of massive clusters to gas expulsion – the cluster density dependence. *Astron. Astrophys.* **555**, A135 (2013).
38. Guszejnov, D. et al. Cluster assembly and the origin of mass segregation in the STARFORGE simulations. *Mon. Not. R. Astron. Soc.* **515**, 167–184 (2022).
39. Kawamura, A. et al. The second survey of the molecular clouds in the large magellanic cloud by NANTEN. II. Star formation. *Astrophys. J. Suppl. Ser.* **184**, 1–17 (2009).
40. Kim, J. et al. PHANGS-JWST first results: duration of the early phase of massive star formation in NGC 628. *Astrophys. J. Lett.* **944**, L20 (2023).
41. Schinnerer, E. & Leroy, A. K. Molecular gas and the star-formation process on cloud scales in nearby galaxies. *Annu. Rev. Astron. Astrophys.* **62**, 369–436 (2024).
42. McLeod, A. F. et al. The impact of pre-supernova feedback and its dependence on environment. *Mon. Not. R. Astron. Soc.* **508**, 5425–5448 (2021).
43. Barnes, A. T. et al. Comparing the pre-SNe feedback and environmental pressures for 6000 H II regions across 19 nearby spiral galaxies. *Mon. Not. R. Astron. Soc.* **508**, 5362–5389 (2021).
44. Della Bruna, L. et al. Stellar feedback in M 83 as observed with MUSE. II. Analysis of the H II region population: Ionisation budget and pre-SN feedback. *Astron. Astrophys.* **666**, A29 (2022).
45. Cerviño, M. & Luridiana, V. Physical limits to the validity of synthesis models. The lowest luminosity limit. *Astron. Astrophys.* **413**, 145–157 (2004).
46. Hennebelle, P. & Grudić, M. Y. The physical origin of the stellar initial mass function. *Annu. Rev. Astron. Astrophys.* **62**, 63–111 (2024).
47. Grudić, M. Y., Guszejnov, D., Hopkins, P. F., Offner, S. S. R. & Faucher-Giguère, C.-A. STARFORGE: towards a comprehensive numerical model of star cluster formation and feedback. *Mon. Not. R. Astron. Soc.* **506**, 2199–2231 (2021).
48. Wainer, T. M. et al. The timescales of embedded star formation as observed in STARFORGE. *Astrophys. J.* **998**, 215 (2026).
49. Kim, J.-G., Kim, W.-T. & Ostriker, E. C. Modeling UV radiation feedback from massive stars. II. Dispersal of star-forming giant molecular clouds by photoionization and radiation pressure. *Astrophys. J.* **859**, 68 (2018).
50. Weidner, C., Kroupa, P. & Bonnell, I. A. D. The relation between the most-massive star and its parental star cluster mass. *Mon. Not. R. Astron. Soc.* **401**, 275–293 (2010).
51. Stanway, E. R. & Eldridge, J. J. Exploring the impact of IMF and binary parameter stochasticity with a binary population synthesis code. *Mon. Not. R. Astron. Soc.* **522**, 4430–4443 (2023).
52. Longmore, S. N. et al. in *Protostars and Planets VI* (eds Beuther, H. et al.) 291–314 (University of Arizona Press, 2014).
53. Winter, A. J. & Haworth, T. J. The external photoevaporation of planet-forming discs. *Eur. Phys. J. Plus* **137**, 1132 (2022).
54. Stolte, A. et al. Circumstellar discs in galactic centre clusters: disc-bearing B-type stars in the quintuplet and arches clusters. *Astron. Astrophys.* **578**, A4 (2015).
55. Pfalzner, S., Dehghani, S. & Michel, A. Most planets might have more than 5 Myr of time to form. *Astrophys. J. Lett.* **939**, L10 (2022).
56. Pineda, J. E. et al. A protostellar system fed by a streamer of 10,500 au length. *Nat. Astron.* **4**, 1158–1163 (2020).
57. Kuffmeier, M., Jensen, S. S. & Haugbølle, T. Rejuvenating infall: a crucial yet overlooked source of mass and angular momentum. *Eur. Phys. J. Plus* **138**, 272 (2023).
58. Gupta, A. et al. TIPSY: Trajectory of Infalling Particles in Streamers around Young stars. Dynamical analysis of the streamers around S CrA and HL Tau. *Astron. Astrophys.* **683**, A133 (2024).
59. Padoan, P., Pan, L., Pelkonen, V.-M., Haugbølle, T. & Nordlund, Å The formation of protoplanetary disks through pre-main-sequence Bondi–Hoyle accretion. *Nat. Astron.* **9**, 862–871 (2025).
60. Haworth, T. J., McCaughrean, M. J., Pearson, S. G. & Booth, R. A. A possible trail of dust from a young, highly extincted brown dwarf in the outskirts of the Trapezium Cluster. *Mon. Not. R. Astron. Soc.* **537**, 3313–3330 (2025).
61. Qiao, L., Coleman, G. A. L. & Haworth, T. J. Planet formation via pebble accretion in externally photoevaporating discs. *Mon. Not. R. Astron. Soc.* **522**, 1939–1950 (2023).
62. Gaia Collaboration Gaia Data Release 3. Summary of the content and survey properties. *Astron. Astrophys.* **674**, A1 (2023).
63. Gregg, B. et al. Feedback in Emerging Extragalactic Star Clusters, FEAST: the relation between 3.3 μm polycyclic aromatic hydrocarbon emission and star formation rate traced by ionized gas in NGC 628. *Astrophys. J.* **971**, 115 (2024).
64. Calzetti, D. et al. JWST-FEAST: Feedback in Emerging extrAgalactic Star clusTers: calibration of star formation rates in the mid-infrared with NGC 628. *Astrophys. J.* **971**, 118 (2024).
65. Whitmore, B. C. et al. PHANGS-JWST first results: massive young star clusters and new insights from JWST observations of NGC 1365. *Astrophys. J. Lett.* **944**, L14 (2023).

66. Oh, S. & Kroupa, P. The influence of stellar dynamical ejections and collisions on the relation between the maximum stellar and star cluster mass. *Mon. Not. R. Astron. Soc.* **424**, 65–79 (2012).
67. Oh, S. & Kroupa, P. Dynamical ejections of massive stars from young star clusters under diverse initial conditions. *Astron. Astrophys.* **590**, A107 (2016).
68. Pfalzner, S. & Kaczmarek, T. The expansion of massive young star clusters – observation meets theory. *Astron. Astrophys.* **559**, A38 (2013).
69. Renzo, M. et al. Massive runaway and walkaway stars. A study of the kinematical imprints of the physical processes governing the evolution and explosion of their binary progenitors. *Astron. Astrophys.* **624**, A66 (2019).
70. Pedrini, A. Data for "Stochasticity matters: the near infrared SED of young star clusters in the FEAST galaxies". *MAST Archive, Space Telescope Science Institute* https://doi.org/10.17909/f4vm-c771 (2025).
71. Adamo, A. & Smith, L. Data from Feedback in Emerging extrAgalactic Star clusTers (FEAST). *MAST Archive, Space Telescope Science Institute* https://doi.org/10.17909/6dc1-9h53 (2025).
72. Astropy Collaboration Astropy: a community Python package for astronomy. *Astron. Astrophys.* **558**, A33 (2013).
73. Van Der Walt, S., Colbert, S. C. & Varoquaux, G. The NumPy Array: a structure for efficient numerical computation. *Comput. Sci. Eng.* **13**, 22–30 (2011).
74. Virtanen, P. et al. SciPy 1.0: fundamental algorithms for scientific computing in Python. *Nat. Methods* **17**, 261–272 (2020).
75. Hunter, J. D. Matplotlib: a 2D graphics environment. *Comput. Sci. Eng.* **9**, 90–95 (2007).
76. pandas-dev/pandas: Pandas (The Pandas Development Team, 2020).
77. Joye, W. A. & Mandel, E. New features of SAOImage DS9. *Astron. Data Anal. Softw. Syst. XII* **295**, 489 (2003).
78. Fahrion, K. & De Marchi, G. Extending the extinction law in 30 Doradus to the infrared with JWST. *Astron. Astrophys.* **671**, L14 (2023).

Acknowledgements

This project is based in part on observations made with the NASA/ESA/CSA JWST, which is operated by the Association of Universities for Research in Astronomy, Inc., under NASA contract NAS 5-03127. These observations are associated with programme no. 1783. Support for programme no. 1783 was provided by NASA through a grant from the Space Telescope Science Institute, which is operated by the Association of Universities for Research in Astronomy, Inc., under NASA contract NAS 5-03127. A.A. and A.P. acknowledge support from the Swedish National Space Agency (SNSA) through grant 2021-00108. A.A. and H.F.V. acknowledge support from SNSA 2023-00260. A.B. acknowledges support from the Swedish National Space Agency (2022-00154). M.R.K. acknowledges support from the Australian Research Council through Laureate Fellowship FL220100020. E.P.A. acknowledges support from NASA ATP grant 80NSSC24K0935. A.D.C. acknowledges the support from a Royal Society University Research Fellowship (URF/R1/19160 and URF/R/241028). T.J.H. acknowledges a Dorothy Hodgkin Fellowship, UKRI guaranteed funding for a Horizon Europe ERC consolidator grant (EP/Y024710/1) and UKRI/STFC grant ST/X000931/1. N.L. was supported by a Gliese Fellowship at the Zentrum für Astronomie, Universität Heidelberg, Germany. K.G. is supported by the Australian Research Council through the Discovery Early Career Researcher Award (DECRA) Fellowship (project number DE220100766) funded by the Australian Government. K.G. is supported by the Australian Research Council through the Discovery Early Career Researcher Award (DECRA) Fellowship (project number DE220100766) funded by the Australian Government. M.C. acknowledges the INFN (Iniziativa specifica TAsP).

Author contributions

A.P. designed and led the data analysis, discussion of the results and wrote the manuscript. A.A. is the principal investigator of the FEAST programme. A.A., D.C. and A.B. contributed in designing the data analysis, the scientific discussion and the drafting of the manuscript. T.J.H. contributed to the discussion on the implications of our results for planet formation theories. B.G.E., M.R.K, H.F.V., E.P.A. and A.A.A. were deeply involved in the discussion and scientific interpretations of the results. S.T.L. designed the cluster SED fitting with `CIGALE`. B.G. produced the continuum-subtracted maps used in this work. V.B. performed the data reduction used in this work. J.E.R. designed the FEAST pipeline for cluster extraction and photometry. G.B., M.C., A.D.C., K.G., N.L., T.S.Y.L., D.L., M.M., G.Ö., E.S., L.J.S., M.T. and all co-authors contributed to writing and refining the manuscript, and participated in the discussion.

Funding

Open access funding provided by Stockholm University.

Competing interests

The authors declare no competing interests.

Additional information

Extended data is available for this paper at https://doi.org/10.1038/s41550-026-02857-y.

Supplementary information The online version contains supplementary material available at https://doi.org/10.1038/s41550-026-02857-y.

Correspondence and requests for materials should be addressed to Alex Pedrini or Angela Adamo.

Peer review information *Nature Astronomy* thanks Hwihyun Kim and the other, anonymous, reviewer(s) for their contribution to the peer review of this work. Peer reviewer reports are available.

[1]Department of Astronomy, Stockholm University and Oskar Klein Center, AlbaNova University Center, Stockholm, Sweden. [2]Department of Astronomy, University of Massachusetts, Amherst, MA, USA. [3]Astronomy Unit, School of Physics and Astronomy, Queen Mary University of London, London, UK. [4]Katonah, NY, USA. [5]Research School of Astronomy and Astrophysics, Australian National University, Stromlo, Australian Capital Territory, Australia. [6]Steward Observatory, University of Arizona, Tucson, AZ, USA. [7]Space Telescope Science Institute, Baltimore, MD, USA. [8]I. Physikalisches Institut, Universität zu Köln, Cologne, Germany. [9]Department of Astrophysics, American Museum of Natural History, New York, NY, USA. [10]Dipartimento di Fisica, Università di Pisa, Pisa, Italy. [11]INFN, Pisa, Italy. [12]INAF – OAS, Osservatorio di Astrofisica e Scienza dello Spazio di Bologna, Bologna, Italy. [13]Cardiff Hub for Astrophysics Research and Technology, School of Physics and Astronomy, Cardiff University, Cardiff, UK. [14]Research School of Astronomy and Astrophysics, Australian National University, Canberra, Australian Capital Territory, Australia. [15]ARC Centre of Excellence for All Sky Astrophysics in 3 Dimensions (ASTRO 3D), Canberra, Australian Capital Territory, Australia. [16]Max-Planck-Institut für Astrophysik, Garching, Germany. [17]Zentrum für Astronomie der Universität Heidelberg, Astronomisches Rechen-Institut, Heidelberg, Germany. [18]IPAC, California Institute of Technology, Pasadena, CA, USA. [19]Gemini Observatory/NSFs NOIRLab, Tucson, AZ, USA. [20]These authors contributed equally: Daniela Calzetti, Arjan Bik, Thomas J. Haworth, Bruce G. Elmegreen, Mark R. Krumholz, Sean T. Linden, Benjamin Gregg, Helena Faustino Vieira, Varun Bajaj, Jenna E. Ryon, Ahmad A. Ali, Eric P. Andersson, Giacomo Bortolini, Michele Cignoni, Ana Duarte-Cabral, Kathryn Grasha, Natalia Lahén, Thomas S.-Y. Lai, Drew Lapeer, Matteo Messa, Göran Östlin, Elena Sabbi, Linda J. Smith, Monica Tosi. ✉e-mail: alex.pedrini@astro.su.se; angela.adamo@astro.su.se

https://doi.org/10.1038/s41550-026-02857-y

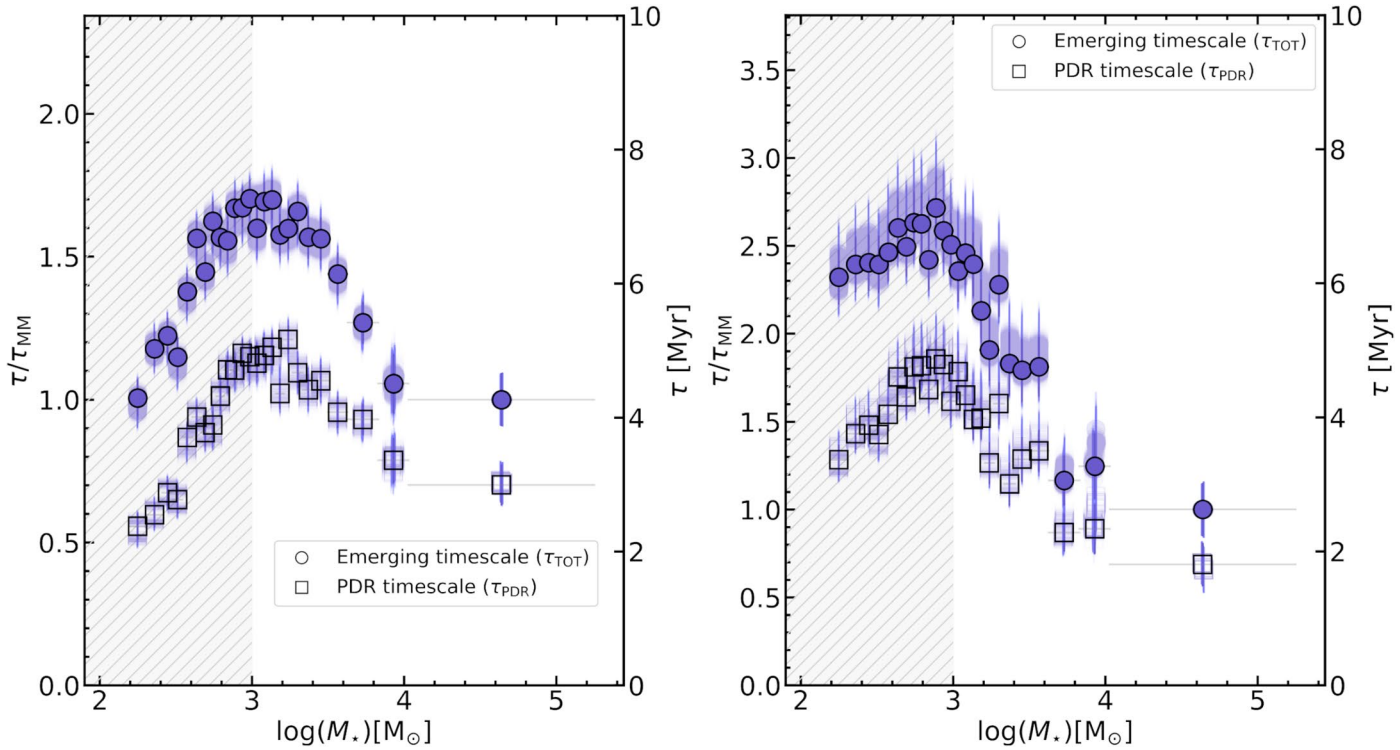

Extended Data Fig. 1 | Emerging timescales as a function of stellar mass in log scale for the combined population of YSCs in the four FEAST galaxies, accounting for stellar mass loss. The left (right) panel shows the scenario in which 20 % (50 %) of the stellar mass is lost during the emerging process from the eYSC to the oYSC phase, as described in the text. Filled circles and open squares indicate the τ_{TOT} and τ_{PDR} timescales, respectively. Each bin contains the same number of objects, except for the largest two mass bins, which are split into two additional bins as described in the text. On the y-axis, τ/τ_{MM} shows timescales normalized to the τ_{TOT} of the highest mass bin, while the secondary y-axis gives absolute values. Shadowed areas beneath the measurements show the timescales re-estimated by randomly sampling the ages of the oYSCs (see Methods). y-error bars show Poisson uncertainties (set by the number of sources in each bin), and x-error bars indicate the bin widths. Below $10^3 M_\odot$, results are affected by completeness limits; this region is shaded in grey.

https://doi.org/10.1038/s41550-026-02857-y

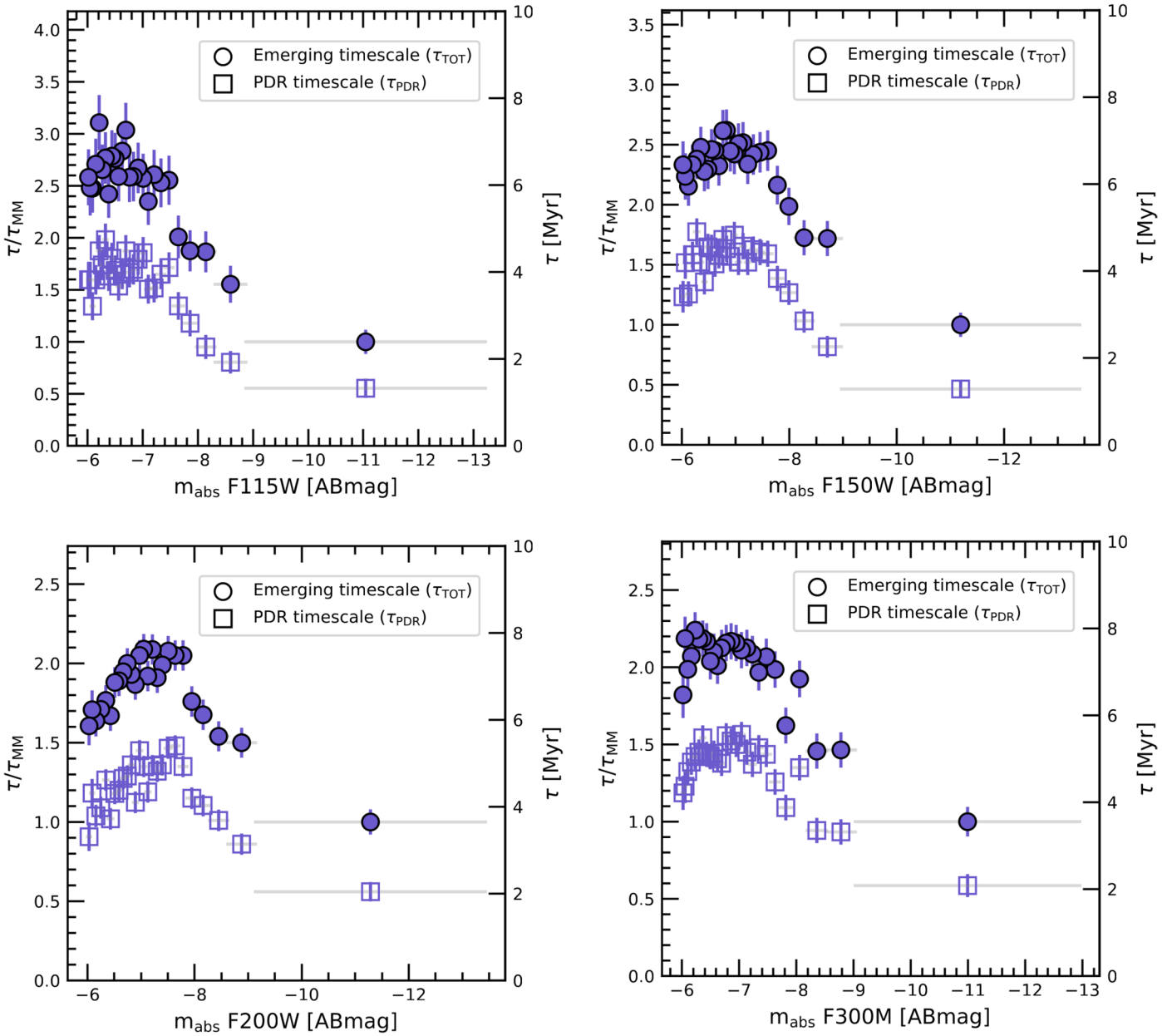

Extended Data Fig. 2 | Emerging timescales as a function of luminosity for the combined population of YSCs in the four FEAST galaxies. The four panels display four different NIRCam filters: F115W (top left), F150W (top right), F200W (bottom left), F300M (bottom right) For each filter, we applied a luminosity cut at $m_{abs} > -6$. Filled circles and open squares indicate the τ_{TOT} and τ_{PDR} timescales, respectively. Each bin contains the same number of objects, except for the largest two luminosity bins, which are split into two additional bins, as described in the text. On the y-axis, for each filter τ/τ_{MM} shows timescales normalized to the τ_{TOT} of the highest luminosity bin, while the secondary y-axis gives absolute values. y-error bars show Poisson uncertainties (set by the number of sources in each bin), and x-error bars indicate the bin widths.